

Generation of ten kilotesla longitudinal magnetic fields in ultraintense laser-solenoid target interactions

K. D. Xiao,¹ C. T. Zhou,^{1,2,3,4,*} H. Zhang,⁴ T. W. Huang,^{2,3} R. Li,¹
B. Qiao,¹ J. M. Cao,^{2,3} T. X. Cai,² S. C. Ruan,^{2,3} and X. T. He^{1,2,4}

¹*Center for Applied Physics and Technology, HEDPS, and School of Physics, Peking University, Beijing 100871, People's Republic of China*

²*Center for Advanced Material Diagnostic Technology, Shenzhen Technology University, Shenzhen 518118, People's Republic of China*

³*College of Optoelectronic Engineering, Shenzhen University, Shenzhen 518060, People's Republic of China*

⁴*Institute of Applied Physics and Computational Mathematics, Beijing 100094, People's Republic of China*

(Dated: March 20, 2018)

Production of the huge longitudinal magnetic fields by using an ultraintense laser pulse irradiating a solenoid target is considered. Through three-dimensional particle-in-cell simulations, it is shown that the longitudinal magnetic field up to ten kilotesla can be observed in the ultraintense laser-solenoid target interactions. The finding is associated with both fast and return electron currents in the solenoid target. The huge longitudinal magnetic field is of interest for a number of important applications, which include controlling the divergence of laser-driven energetic particles for medical treatment, fast-ignition in inertial fusion, etc., as an example, the well focused and confined directional electron beams are realized by using the solenoid target.

Huge magnetic field generation in laboratory has attracted more and more attention due to its wide applications, including plasma physics[1], laboratory astrophysics[2], atomic and nuclear physics[3], and material sciences[4], etc. In laser driven inertial confinement fusion, the huge magnetic field, which is generated by the magnetic flux compression of the seed field, increases the plasma temperature of the hot spot and confines the alpha particles to the burn region[5].

At present, the strongest continuous magnetic field generated by the hybrid magnet is around 45 T, and the strongest pulsed magnetic field generated by the non-destructive electromagnet is around 100 T[6]. Besides of the magnet, high power lasers have the potential to generate huge magnetic fields of extreme strengths. The magnetic field generated by a nanosecond laser ablation on a capacitor-coil target is reported 1.5 kT at the GEKKO-XII laser facility[7], 800 T at the LULI pico 2000 laser facility[8], and 610 T at the GEKKO-LFEX laser facility[9]. The magnetic field 205 T is reported to be generated by the open-ended coil at the SG-II laser facility[10]. With the rapid development of the laser technologies, the laser facilities with higher intensities ($10^{19} \sim 10^{21} \text{W/cm}^2$) and shorter durations (picoseconds to femtoseconds) have been built up[11–13]. When such an ultraintense laser pulse interacts with plasmas, a large number of hot electrons are produced by the laser ponderomotive acceleration. These hot electrons generate currents at the plasma-vacuum interfaces with magnitude $10^{16} \sim 10^{18} \text{A/m}^2$ [14, 15]. The interface currents further induce a huge magnetic field with strength $10^3 \sim 10^5 \text{T}$ [16–22], which is much higher than that from the capacitor-coil with normal discharging currents[23].

Thus, the huge magnetic field of extreme strength can be expected when an ultraintense laser pulse interacts with a specially designed target.

In this Letter, we propose to use an ultraintense laser pulse irradiating solenoid target to generate the huge longitudinal magnetic field, where such target design has also been applied on proton acceleration[24]. The solenoid target consists of a foil and a curved plasma wire. The longitudinal static magnetic fields are induced by the surface currents along the plasma wire and enhanced inside the solenoid, finally achieving almost uniform spatial distribution. Three-dimensional particle-in-cell (PIC) simulations are performed to study the generation of the longitudinal magnetic field inside the solenoid target. As an application, the magnetic field effects on guiding and focusing of the hot electron beams are also studied. The PIC simulation technique has been the main tool for studying laser-plasma interaction and transport of electrons in hot, mildly dense plasma near the relativistic critical density. For simulating overdense plasmas one can use hybrid techniques [25–28], where high-temperature Spitzer resistivity and low-temperature modifications are included. Here we shall use the EPOCH code [29], which have been shown to yield good results in similar laser-plasma interaction problems [30–32].

The solenoid target consists of a foil and a curved plasma wire, as shown in Fig. 1(a). The front of the plasma wire is attached at the rear surface of the foil. The PIC simulation starts from an ionized plasma composed of Cu^{2+} ions and electrons. The electron number density of the target is $n_{e0} = 40n_c$, where $n_c = m_e \epsilon_0 \omega_0^2 / e^2 \approx 1.11 \times 10^{27} \text{m}^{-3}$ is the critical density. The initial temperatures are 1 keV for the electrons and 170 eV for the ions. The diameter and thickness of the foil are $12 \mu\text{m}$ and $1 \mu\text{m}$, respectively. The diameter and longitudinal length of the solenoid are $d = 8 \mu\text{m}$

* Electronic mail: zcangtao@sztu.edu.cn

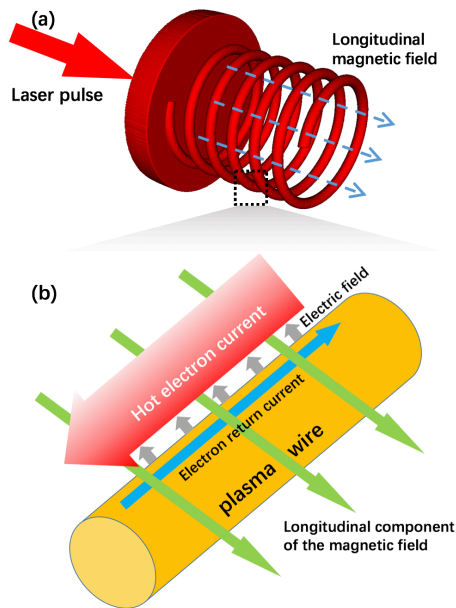


FIG. 1. (Color online) (a) Configuration of the solenoid target, where a curved plasma wire is attached at the backside of a foil. The laser pulse irradiates from the left onto the foil front surface. A backward longitudinal magnetic field is generated inside the solenoid. (b) Schematic diagram of the generation of the surface electric and magnetic fields. A small part of the plasma wire is enlarged. The directions of the currents and fields are denoted by arrows. See context for detail.

and $h = 10 \mu\text{m}$, respectively. The number of coils contained in the solenoid is $n = 6$. The length of a single coil is $l = \sqrt{(\pi d)^2 + (h/n)^2} = 25 \mu\text{m}$, and the total length of the solenoid is $L = 150 \mu\text{m}$. The diameter of the plasma wire is $0.6 \mu\text{m}$. A small scale preplasma is taken in front of the foil with total length $5 \mu\text{m}$ and density profile $n_e = n_{e0} \exp(x/\delta)$, where $\delta = 0.5 \mu\text{m}$. The laser pulse is y -polarized with intensity $2 \times 10^{20} \text{ W/cm}^2$ ($a_0 \approx 12.8$) and duration 100 fs. The laser wave length is $\lambda_0 = 1.06 \mu\text{m}$. The spatial profile of the laser is Gaussian $a = a_0 \exp(-r^2/\sigma^2)$ with the spot radius $\sigma = 3 \mu\text{m}$. The temporal profile of the laser is flat top with raising and falling times of 1 laser cycle. The simulation box size at the $x \times y \times z$ directions are $23 \mu\text{m} \times 16 \mu\text{m} \times 16 \mu\text{m}$, respectively. The number of grids are $1143 \times 795 \times 795$, respectively. The grid length equals to 1 plasma skin depth 20 nm. There is 6 macroparticles filled in each target cell. The laser injection and open boundary conditions are taken at the positive and negative x boundaries, respectively. The periodic boundary conditions are taken at the y and z boundaries.

When the ultraintense laser pulse irradiates the foil front surface, a significant amount of hot electrons are created and accelerated [11]. These hot electrons transit through the foil and some of them enter the curved plasma wire and propagate along the latter as hot electron currents. Because of the Alfvén limit, cold return

currents for balancing the hot electrons are generated, as shown in Fig. 1(b). The hot and return currents at the wire surface form a two-layer structure, inducing a huge surface magnetic field. The hot electron currents gradually expand into the vacuum, so that the spatial distribution of the magnetic field spread towards the center of the solenoid. The magnetic field strength at the center of the solenoid is enhanced by the merging of the expanding fields. The spatial distributions of the magnetic field and the force lines are shown in Fig. 2 at a time when the laser pulse is over. The magnetic fields originating from the plasma wires have merged into a field surrounding the solenoid. The magnetic field lines inside and outside the solenoid are in opposite directions, as can be seen in Figs. 2(b) and (c). The longitudinal magnetic field inside the solenoid is almost uniformly distributed, as shown in Figs. 2(d) and (e). The field strength is about $1 \times 10^4 \text{ T}$ at the solenoid center and about $2 \times 10^4 \text{ T}$ at the plasma wire surface. The evolution of the magnetic field is shown in the insert of Fig. 2(d). The magnetic field strength increases almost linearly in the early time and reaches its maximum value at $t = 300 \text{ fs}$. After that, the magnetic field strength stays at the maximum value with slow decrease for about 100 fs, which is nearly the same as the laser pulse duration. The magnetic field begins to vanish at $t = 400 \text{ fs}$, when the hot electrons almost reach the solenoid end. At $t = 500 \text{ fs}$, the magnetic field strength inside the solenoid is about 6000 T.

The hot electron propagation along the plasma wire is the key mechanism for generation of the longitudinal magnetic field. The energy distribution of wire electrons are shown in Fig. 3 (a). We note that most of the hot electrons moving along the plasma wire have the energies around 5 MeV, and the maximum electron energy is about 20 MeV. With the electron propagation, a surface electric field surrounding the plasma wire is induced, with maximum strength of about $7 \times 10^{12} \text{ V/m}$, as shown in Figs. 3(c) and (d). The electric field can be estimated by $E \approx T_h/eK$, where $T_h \approx 0.511[(1 + I_{18}\lambda_0^2/2)^{1/2} - 1]\text{MeV}$ is the hot-electron temperature and K is the hot-electron spatial extension. The distribution of the two-layer electron currents are shown in Fig. 3(b) with the maximum current density of about $1 \times 10^{17} \text{ A/m}^2$. From the electron current distribution, the strength of the magnetic field at the wire surface can be estimated by $B_{\text{MG}} \approx 0.38n_{29}P_{\text{TW}}^{-1}T_{h,511}R_{\mu\text{m}}T_{c,\text{keV}}[25]$, where n_{29} is the electron density in units of 10^{29} m^{-3} , P_{TW} is the power of the hot electron beam in TW, $T_{h,511}$ is the hot electron temperature in units of 511 keV, $R_{\mu\text{m}}$ is the hot electron beam radius in μm , and $T_{c,\text{keV}}$ is the cold background electron temperature in units of keV. In the simulations, the hot and cold electron temperatures are about 4.6 MeV and 250 keV respectively. The electron beam intensity along the wire is about $P_e \sim \frac{c}{\Delta L} \sum_{\Delta L} \epsilon_e \approx 0.1 \text{ TW}$, where ϵ_e is the electron energy for the electrons in wire with length ΔL . The beam electron density is nearly $8 \times 10^{27} \text{ m}^{-3}$ and the R is taken as the plasma wire radius $0.3 \mu\text{m}$. From the

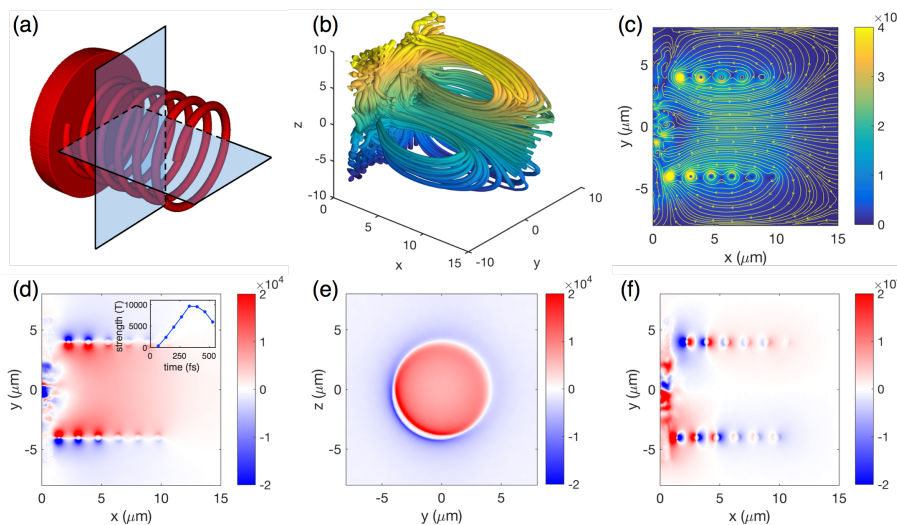


FIG. 2. (Color online) (a) Positions of two cross-section planes, which are x - y plane ($z = 0$ plane) and y - z plane ($x = 5$ μm plane). (b) Three-dimensional distribution of the magnetic field lines. The lines facing forward are hidden to look inside. The laser pulse is from the left along the x -axis. (c) Magnetic force lines in the x - y plane. (d, e) B_x in the x - y and y - z planes. (f) B_y in the x - y plane. The magnetic fields are taken at $t = 330$ fs and their unit is T. Evolution of B_x at $(5, 0, 0)$ (μm) is shown in the insert of (d).

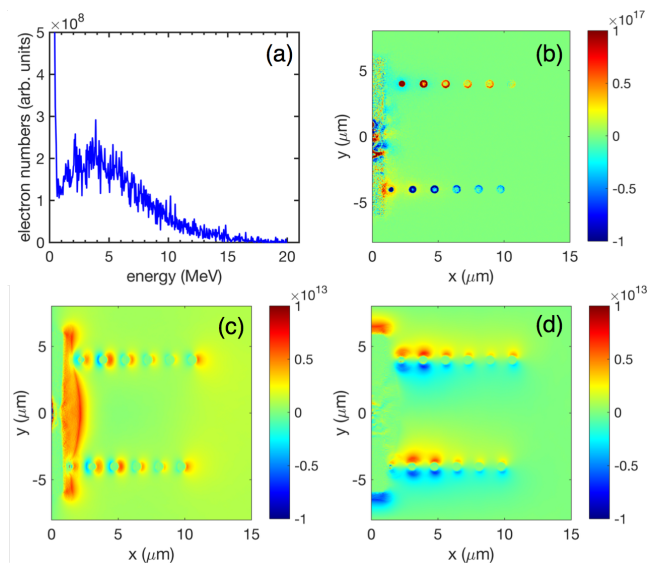


FIG. 3. (Color online) Distribution of the currents and electric fields. (a) Spectrum for electrons in the plasma wire from $x = 2$ μm to 10 μm . (b) Distribution of the electron current j_z , (c) the longitudinal electric field E_x , and (d) the transverse electric field E_y at the cross-section plane x - y ($z = 0$ plane). The spectrum and distributions are for $t = 330$ fs. The units for the electron current and electric fields are A/m^2 and V/m , respectively.

above equation, the estimated magnetic field strength at the wire surface is about 205 MG (2×10^4 T), which agrees with our simulation result.

The relativistic electron beam (REB) has been widely used in laser driven proton and radiation sources, iso-

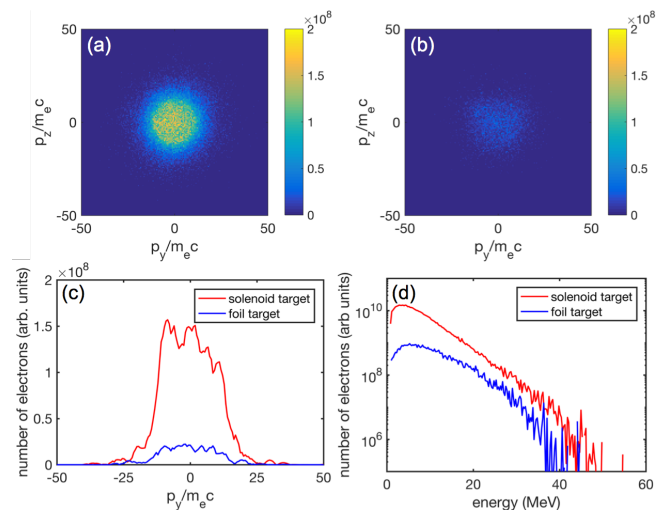


FIG. 4. (Color online) Time integral (from $t = 0$ to 500 fs) of the electron numbers passing through a disc placed 8 μm behind the foil. The disc radius is 5 μm . (a) Distribution of electron transverse momentum space for the electrons with energies greater than 5 MeV for the solenoid target, and (b) the bare foil target. (c) Corresponding transversal distribution of the two momentum space. (d) Electron spectrum for the time integral.

choric heating of materials, and warm dense matter production, etc.[33–36]. In previous work[22, 37], ones used externally longitudinal magnetic fields to focus and guide the REB. Here we consider an integrated simulation to simulate simultaneously generate both the collimating magnetic fields and the REB using the solenoid target. In the solenoid, an electron in x - y plane is affected by

the force $F_z = ev_y B_x - ev_x B_y$. After a time interval of Δt , the z component of the electron velocity is $v_z = \frac{e}{m} B_x S_y - \frac{e}{m} B_y S_x$, where the magnetic field strength is assumed constant during the small time interval, and S_x and S_y are the electron displacements at the x and y directions, respectively. This transverse velocity v_z leads to a focusing force $F_y = -\frac{e^2}{m} B_x^2 S_y + \frac{e^2}{m} B_x B_y S_x$. For a given magnetic field $B_x = 1 \times 10^4$ T, the maximum energy of the focused electron is $\mathcal{E}_y \sim \frac{e^2}{m} B_x^2 S_y^2 \approx 17.6$ MeV with focusing length $S_y = 1 \mu\text{m}$, and $\mathcal{E}_y \sim 70.3$ MeV with $S_y = 2 \mu\text{m}$. To see the REB focusing effect of the solenoid target, we have compared the electron divergence of this target with that of a normal bare foil target. The distribution of electrons passing through a time integral disc placed $8 \mu\text{m}$ behind the front foil for the two cases is shown in Fig. 4. The disc radius is $5 \mu\text{m}$. Figs. 4(a) and (b) show that for the bare foil target the REB diverges behind the foil and for the solenoid target it is confined and focused by the magnetic field. A large number of hot electrons are trapped by the solenoid magnetic field, forming a dense electron cloud at the center of the momentum space, as shown in Fig. 4(c). The electron spectrums for the two cases are shown in Fig. 4(d). It is seen that the total hot electron number and the maximum electron energy in the solenoid target is higher than that for the bare foil target. Since the laser-foil interactions are same in the two cases, the difference in the electron spectrum is related to the electron motion behind the foil. In the solenoid target case more electrons

pass through the disc, while in bare foil target case a large number of electrons are diverged out of the disc. As a result, the REB generated by using the solenoid target has large electron number and low divergence, and is well confined and guided by the longitudinal magnetic field.

In summary, generation of huge longitudinal magnetic field can be achieved by using a solenoid target. In our three-dimensional particle-in-cell simulation, magnetic fields of strength nearly 1×10^4 T and duration nearly 500 fs is generated by a laser pulse of intensity 2×10^{20} W/cm² and duration 100 fs. In this scheme, the laser heated hot electrons flow along the solenoid plasma wire, generating surface electric fields, and forming interface hot electron currents and cold return currents. The two-layer currents further induce the longitudinal magnetic field. The magnetic field is nearly uniform distributed inside the solenoid, and the strength is far beyond the traditional nanosecond laser-coil interaction methods. As an application, the focusing and guiding of the hot electron beams by the solenoid magnetic field is also studied.

This work is supported by the National Key Program for S&T Research and Development, Grant No.2016YFA0401100; the SSTDF, Grant No. JCYJ20160308093947132; the National Natural Science Foundation of China (NSFC), Grant Nos. 11575031, 11575298, 91230205, and 11705120. B. Q. acknowledges the support from Thousand Young Talents Program of China.

-
- [1] E. Liang, K. Nishimura, H. Li, and S. P. Gary, *Phys. Rev. Lett.* **90**, 085001 (2003).
- [2] A. Ciardi, T. Vinci, J. Fuchs, B. Albertazzi, C. Riconda, H. Pépin, and O. Portugall, *Phys. Rev. Lett.* **110**, 025002 (2013).
- [3] B. N. Murdin, J. Li, M. L. Y. Pang, E. T. Bowyer, K. L. Litvinenko, S. K. Clowes, H. Engelkamp, C. R. Pidgeon, I. Galbraith, N. V. Abrosimov, H. Riemann, S. G. Pavlov, H-W. Hübers, and P. G. Murdin, *Nat. Comm.* **4**, 1469 (2013).
- [4] E. Kojima, A. Miyata, Y. Motome, H. Ueda, Y. Ueda, and S. Takeyama, *J. Low. Temp. Phys.* **159**, 3 (2010).
- [5] P. Y. Chang, G. Fiksel, M. Hohenberger, J. P. Knauer, R. Betti, F. J. Marshall, D. D. Meyerhofer, F. H. Séguin, and R. D. Petrasso, *Phys. Rev. Lett.* **107**, 035006 (2011).
- [6] I. M. Hayes, R. D. McDonald, N. P. Breznay, T. Helm, P. J. W. Moll, M. Wartenbe, A. Shekhter, and J. G. Analytis, *Nat. Phys.* **12**, 916 (2016).
- [7] S. Fujioka, Z. Zhang, K. Ishihara, K. Shigemori, Y. Hironaka, T. Johzaki, A. Sunahara, N. Yamamoto, H. Nakashima, T. Watanabe, H. Shiraga, H. Nishimura, and H. Azechi, *Sci. Reports* **3**, 1170 (2013).
- [8] J. J. Santos, M. Bailly-Grandvaux, L. Giuffrida, P. Forestier-Colleoni, S. Fujioka, Z. Zhang, P. Korneev, R. Bouillaud, S. Dorard, D. Batani, M. Chevrot, J. E. Cross, R. Crowston, J-L. Dubois, J. Gazave, G. Gregori, E. d'Humières, S. Hulin, K. Ishihara, S. Kojima, E. Loyez, J-R. Marquès, A. Morace, P. Nicolai, O. Peyrusse, A. Poyé, D. Raffestin, J. Ribolzi, M. Roth, G. Schaumann, F. Serres, V. T. Tikhonchuk, P. Vacar, and N. Woolsey, *New J. Phys.* **17**, 083051 (2015).
- [9] K. F. F. Law, M. Bailly-Grandvaux, A. Morace, S. Sakata, K. Matsuo, S. Kojima, S. Lee, X. Vaisseau, Y. Arikawa, A. Yogo, K. Kondo, Z. Zhang, C. Bellei, J. J. Santos, S. Fujioka, and H. Azechi, *Appl. Phys. Lett.* **108**, 091104 (2016).
- [10] B. J. Zhu, Y. T. Li, D. W. Yuan, Y. F. Li, F. Li, G. Q. Liao, J. R. Zhao, J. Y. Zhong, F. B. Xue, S. K. He, W. W. Wang, F. Lu, F. Q. Zhang, L. Yang, K. N. Zhou, N. Xie, W. Hong, H. G. Wei, K. Zhang, B. Han, X. X. Pei, C. Liu, Z. Zhang, W. M. Wang, J. Q. Zhu, Y. Q. Gu, Z. Q. Zhao, B. H. Zhang, G. Zhao, and J. Zhang, *Appl. Phys. Lett.* **107**, 261903 (2015).
- [11] A. Pukhov, *Rep. Prog. Phys.* **65**, R1-R55 (2002).
- [12] H. Daido, M. Nishiuchi, and A. S. Pirozhkov, *Rep. Prog. Phys.* **75**, 056401 (2012).
- [13] A. Macchi, M. Borghesi, and M. Passoni, *Rev. Mod. Phys.* **85**, 751 (2013).
- [14] T. Nakamura, S. Kato, H. Nagatomo, and K. Mima, *Phys. Rev. Lett.* **93**, 265002 (2004).
- [15] C. T. Zhou, L. Y. Chew, and X. T. He, *Appl. Phys. Lett.* **97**, 051502 (2010).
- [16] M. G. Haines, *Phys. Rev. Lett.* **78**, 254 (1997).
- [17] A. R. Bell, J. R. Davies, and S. M. Guerin, *Phys. Rev. E*

- 58**, 2471 (1998).
- [18] G. Sarri, A. Macchi, C. A. Cecchetti, S. Kar, T. V. Liseykina, X. H. Yang, M. E. Dieckmann, J. Fuchs, M. Galimberti, L. A. Gizzi, R. Jung, I. Kourakis, J. Osterholz, F. Pegoraro, A. P. L. Robinson, L. Romagnani, O. Willi, and M. Borghesi, *Phys. Rev. Lett.* **109**, 205002 (2012).
- [19] S. Kar, A. P. L. Robinson, D. C. Carroll, O. Lundh, K. Markey, P. McKenna, P. Norreys, and M. Zepf, *Phys. Rev. Lett.* **102**, 055001 (2009).
- [20] M. Tatarakis, I. Watts, F. N. Beg, E. L. Clark, A. E. Dangor, A. Gopal, M. G. Haines, P. A. Norreys, U. Wagner, M. S. Wei, M. Zepf, and K. Krushelnick, *Nature* **415**, 280 (2002).
- [21] B. Ramakrishna, S. Kar, A. P. L. Robinson, D. J. Adams, K. Markey, M. N. Quinn, X. H. Yuan, P. McKenna, K. L. Lancaster, J. S. Green, R. H. H. Scott, P. A. Norreys, J. Schreiber, and M. Zepf, *Phys. Rev. Lett.* **105**, 135001 (2010).
- [22] F. Pérez, A. Debayle, J. Honrubia, M. Koenig, D. Batani, S. D. Baton, F. N. Beg, C. Benedetti, E. Brambrink, S. Chawla, F. Dorchies, C. Fourment, M. Galimberti, L. A. Gizzi, L. Gremillet, R. Heathcote, D. P. Higginson, S. Hulin, R. Jafer, P. Koester, L. Labate, K. L. Lancaster, A. J. MacKinnon, A. G. MacPhee, W. Nazarov, P. Nicolai, J. Pasley, R. Ramis, M. Richetta, J. J. Santos, A. Sgattoni, C. Spindloe, B. Vauzour, T. Vinci, and L. Volpe, *Phys. Rev. Lett.* **107**, 065004 (2011).
- [23] H. Daido, F. Miki, K. Mima, M. Fujita, K. Sawai, H. Fujita, Y. Kitagawa, S. Nakai, and C. Yamanaka, *Phys. Rev. Lett.* **56**, 846 (1986).
- [24] S. Kar, H. Ahmed, R. Prasad, M. Cerchez, S. Brauckmann, B. Aurand, G. Cantono, P. Hadjisolomou, C. L. S. Lewis, A. Macchi, G. Nersisyan, A. P. L. Robinson, A. M. Schroer, M. Swantusch, M. Zepf, O. Willi, and M. Borghesi, *Nat. Comm.* **7**, 10792 (2015).
- [25] A. R. Bell, and R. J. Kingham, *Phys. Rev. Lett.* **91**, 035003 (2003).
- [26] A. P. L. Robinson, M. Sherlock, and P. A. Norreys, *Phys. Rev. Lett.* **100**, 025002 (2008); A. P. L. Robinson, M. H. Key, and M. Tabak, *Phys. Rev. Lett.* **108**, 125004 (2012).
- [27] R. B. Campbell, R. Kodama, K. A. Tanaka, and D. R. Welch, *Phys. Rev. Lett.* **84**, 055001 (2005).
- [28] I. R. Davies, *Phys. Rev. E* **68**, 056404 (2003).
- [29] T. D. Arber, K. Bennett, C. S. Brady, A. Lawrence-Douglas, M. G. Ramsay, N. J. Sircombe, P. Gillies, R. G. Evans, H. Schmitz, A. R. Bell, and C. P. Ridgers, *Plasma Phys. Controlled Fusion* **57**, 113101 (2015).
- [30] F. Zamponi, A. Lübcke, T. Kämpfer, I. Uschmann, E. Förster, A. P. L. Bobinson, A. Giuletta, P. Köster, L. Labate, T. Levato, and L. A. Gizzi, *Phys. Rev. Lett.* **105**, 085001 (2010).
- [31] C. P. Ridgers, C. S. Brady, R. Ducloux, J. G. Kirk, K. Bennett, T. D. Arber, A. P. L. Robinson, and A. R. Bell, *Phys. Rev. Lett.* **108**, 165006 (2012).
- [32] M. Cerchez, A. L. Giesecke, C. Peth, M. Toncian, B. Albertazzi, J. Fuchs, O. Willi, and T. Toncian, *Phys. Rev. Lett.* **110**, 065003 (2013).
- [33] A. Macchi, M. Borghesi, and M. Passoni, *Rev. Mod. Phys.* **85**, 751 (2013).
- [34] S. Corde, K. Ta Phuoc, G. Lambert, R. Fitour, V. Malka, A. Rousse, A. Beck and E. Lefebvre, *Rev. Mod. Phys.* **85**, 1 (2013).
- [35] F. Pérez, L. Gremillet, M. Koenig, S. D. Baton, P. Audebert, M. Chahid, C. Rousseaux, M. Drouin, E. Lefebvre, T. Vinci, J. Rassuchine, T. Cowan, S. A. Gaillard, K. A. Flippo, and R. Shepherd, *Phys. Rev. Lett.* **104**, 085001 (2010).
- [36] P. Norreys, D. Batani, S. Baton, F. N. Beg, R. Kodama, P. M. Nilson, P. Patel, F. Pérez, J. J. Santos, R. H. H. Scott, V. T. Tikhonchuk, M. Wei and J. Zhang, *Nucl. Fusion* **54**, 054004 (2014).
- [37] M. Bailly-Grandvaux, J. J. Santos, C. Bellei, P. Forestier-Colleoni, S. Fujioka, L. Giuffrida, J. J. Honrubia, D. Batani, R. Bouillaud, M. Chevrot, J.E. Cross, R. Crowston, S. Dorard, J.-L. Dubois, M. Ehret, G. Gregori, S. Hulin, S. Kojima, E. Loyez, J.-R. Marquès, A. Morace, Ph. Nicolai, M. Roth, S. Sakata, G. Schaumann, F. Serres, J. Servel, V. T. Tikhonchuk, N. Woolsey and Z. Zhang, *Nat. Comm.* **9**, 102 (2018).